Two-phase viscous modeling of compaction of granular materials

Joseph M. Powers[a]
Department of Aerospace and Mechanical Engineering, University of Notre Dame, Notre Dame, Indiana 46556-5637

An inviscid model for deflagration-to-detonation transition in granular energetic materials is extended by addition of explicit intraphase momenta and energy diffusion so as to (1) enable the use of a straightforward numerical scheme, (2) avoid prediction of structures with smaller length scales than the component grains, and (3) have a model prepared to describe long time scale transients that are present in some slow processes which can lead to detonation. The model is shown to be parabolic, frame invariant, and dissipative. Consideration of the characteristics for cases with and without intraphase diffusion indicate what boundary conditions are necessary for a well posed problem. A simple numerical method, based on a method of lines applied to the nonconservative form of the equations, is shown to predict convergence at the proper rate to unique solutions which agree well with known solutions for an unsteady inviscid shock tube and a steady piston-driven viscous shock. A series of simulations of inert piston-driven subsonic compaction waves in which the additional mechanisms of interphase compaction, drag, and heat transfer are systematically introduced at an order of magnitude suggested by experiments reveals that interphase drag and heat transfer equilibrate velocities and temperatures, and that compaction equilibrates solid and configurational stresses. At higher piston velocities, supersonic shock and compaction waves are induced; comparison of predictions with and without viscosity demonstrate some of the computational advantages of explicit inclusion of diffusion. The local dissipation rates for each mechanism are quantified, and it is seen that dissipation due to compaction dominates that due to intraphase and interphase transport of linear momenta and energy, suggesting that compaction is the key mechanism in inducing the transition to detonation in piston-driven experiments. © *2004 American Institute of Physics.* [DOI: 10.1063/1.1764951]

I. INTRODUCTION

Common heterogeneous energetic solids such as the Plastically Bound eXplosive PBX 9501, composed of granular crystalline HMX (cyclotetramethylene-tetranitramine) embedded within a polymeric binder, contain grains with length scales on the order 100 μm. A computational model which captures the grain scale details thus requires cell sizes on the order of 1 μm, as well as complex models for grain/binder interfaces. Such an approach is clearly impractical for systems whose length scales are typical for engineering applications; these are on the order of 10 cm or greater. However it is also well known that features of macroscale engineering interest, such as susceptibility to detonation, are strong functions of the microscale granularity.[1,2] Consequently, given the resources of present computational technology, a successful theory to predict the behavior of these granular materials at engineering length scales will most likely need to employ a continuum theory with specialized nontraditional constitutive models which capture effects present at the granular scale.

Inviscid continuum mixture theories have been used for over two decades to model compaction and the transition to detonation in granular energetic materials.[3–21] Following the work of Baer and Nunziato,[5] most studies now focus on models which are formally hyperbolic. Such models are well posed for initial value problems and admit a variety of discontinuous waves. However, most incarnations of these models cannot be written in full conservation form, which gives rise to difficulties in properly capturing the discontinuities with standard numerical methods.[19] Moreover, as noted by Powers *et al.*,[9] common constitutive models for interphase mass, momenta, and energy transport can predict, when carefully resolved, flow structures with length scales that are encroaching those for which the continuum assumption is invalid for the granular mixtures. These models have typically been applied to predict results of experiments in which a piston is driven at high velocity into an ambient bed of tightly packed granular material. In such experiments, it is presumed that diffusion will have insufficient time to act on the macroscales and is thus not modeled. However, it is clear that *some* mechanism must be included in the continuum mixture theory to model the subcontinuum effects of granularity. Commonly used algebraic interphase transport terms have appeal, but as they are represented as source terms and not diffusion terms, they have limited ability to suppress fine-scale physical and numerical instabilities, such as the Kelvin–Helmholtz instability, which is present near slip lines. Moreover, there is another important class of problems in which a granular energetic solid is subjected to a slow

[a]Electronic mail: powers@nd.edu

2975

incubation, which could be on the order of hours, in which diffusion plays a key role. In this process, known as cookoff, it is conjectured that the material goes through stages in which first diffusion, then slow convection, granular compaction, and lastly acoustic wave steepening lead finally to catastrophic detonation. In order to have a robust model, amenable to straightforward numerical analysis, which is able to account for all of these mechanisms, as well as to provide a mechanism to suppress subcontinuum length scales predicted by common inviscid models, a viscous extension of the earlier models is studied here.

The new viscous model is most directly extended from the inviscid model given by Bdzil et al.,[14] which will be called here the BMSKS model. As detailed in their article, the BMSKS model has several subtle but compelling advantages over related models, most importantly embodied in its careful analysis of the second law of thermodynamics, especially as related to the process of compaction of the granular material, as well as its thermodynamically consistent use of a solid equation of state with explicit dependence on volume fraction. BMSKS employ an overly general form for interphase transport terms in order to demonstrate that the second law admits a wider class of constitutive theories than had been demonstrated previously. We have made specific choices, admitted by the BMSKS model, so as to (1) include so-called nozzling effects, which helps insure second law satisfaction and admits the plausible, albeit *ad hoc*, physical justification given by BMSKS, (2) assign all so-called compaction work to the solid, (3) deposit all energy released by reaction to the gas phase, (4) require Galilean frame invariance, (5) assign all dissipation from interphase drag to the gas phase, and (6) neglect dissipation introduced by velocity changes associated with interphase mass transport, These choices correspond, in the notation described by BMSKS, to $w=1$, $b=0$, $\nu=1$, $f=1$, $a=0$, and $\alpha=0$.

As discussed by BMSKS, inclusion of nozzling effects introduces an asymmetry in the two-phase equations which renders it impossible to cast the equations in a fully conservative form. This has important implications for analytic and, consequently, computational solutions involving discontinuities, as has been extensively discussed in the literature; a recent summary is given by Kapila et al.[19] Importantly, a so-called regularization is needed to fully specify shock jumps. Computation of end states of jumps by standard numerical methods constructed to be flux conservative is easily corrupted by numerical errors, in contrast to models which are formally conservative. The study of Abgrall and Saurel[20] most completely addresses this issue within the context of traditional flux-conservative numerical methods; however, the fundamental nonconservative nature of the underlying theory removes the foundation upon which most common high resolution shock capturing schemes are based. Consequently, in that extreme care must be used in constructing a numerical method for such models, it is reasonable to explore alternatives. Kapila et al.[19] suggest three viable remedies: (1) asymptotic analysis of inner layers to yield the appropriate jumps, (2) development of a physically based model for grain-scale phenomena, or (3) careful imposition of a simple diffusion model, motivated in part by the work of

Sainsaulieu,[22] to simulate the grain-scale physics, and focus their efforts on the first. Here, we will consider the third.

We have extended the BMSKS model in three ways. First, the equations are written in a general three-dimensional tensorial form, and are thus suited to arbitrary geometries. Second, relatively simple, thermodynamically consistent state equations with sufficient nonideality to capture gross features observed in acoustic and compaction wave dynamics experiments have been selected. And third, intraphase momenta and energy diffusion effects have been included in a simplistic fashion, motivated by traditional diffusion in gas-phase systems; these models amount to the assumption of materials which behave as Newtonian fluids which satisfy Fourier's law. In the same sense that molecular collision theory can be used to predict values for diffusion coefficients in gaseous systems, one can imagine that a granular-scale submodel could be used to give rational estimates for macroscale diffusion in these systems. We are at present developing such a theory, which is not reported here. In the present study, a simple and practical choice for diffusion coefficients is made so as to insure that the finest length scales predicted by the model are large enough to encompass several grains. Once this choice of diffusion coefficients is made, it is adhered to. One is then obliged to include a sufficient number of computational cells to insure that the diffusion induced by the physical mechanism dominates the diffusion induced by the chosen numerical method. Further, one need not then be concerned if the computational cell size approaches or is less than the grain size, since the actual viscous structure encompasses many grains.

An advantage of choosing a simple model for diffusion is that it is easy to design to prevent grain-scale structures from being predicted. The disadvantage of this choice is that the diffusion coefficients necessary to achieve this result are significantly higher than those appropriate to describe macroscale diffusion in a slow cookoff process, not simulated here. However, one can imagine a straightforward extension to craft a grid-independent, grain size-dependent diffusion model in which the diffusion coefficients had strain rate dependency so as to guarantee ordinary diffusion at low strain rates found in cookoff, and high values in regions of steep gradients near shocks.

It is appropriate to give an extended comment on numerical diffusion, i.e., pseudodiffusion proportional to the grid discretization length scale and an intrinsic property of the discretization scheme. Here the term "numerical diffusion" is used loosely and actually encompasses all numerical noise-generating mechanisms, the most prominent typically being diffusion and dispersion. It is often argued that inviscid models are sufficient because numerical diffusion, harnessed wisely at a super-granular scale, will be sufficient to properly smear subcontinuum effects. However, when one realizes that the amount of numerical diffusion present in all stable shock capturing schemes is highly dependent on the particular method chosen, and that it is often difficult to quantify the amount of numerical diffusion, one concludes that alternatives have some clear advantages. First, models with explicit, grid-independent diffusion are more likely to converge when subjected to grid resolution tests. Grid resolution tests ap-

plied to inviscid models soon bring the model to the sub-granular level, where it is unphysical. Furthermore, in multidimensional inviscid calculations, it is obvious that grid resolution in the neighborhood of structures such as Kelvin–Helmholtz instabilities can never converge, as ever-finer grids reveal ever-finer fractal-like structures. Consequently, it is more reliable to employ explicit, grid-independent diffusion so as to provide a clear mechanism to suppress nonphysical high frequency instabilities, as well as to provide a means by which the solution to which one converges is independent of the particular numerical method chosen. Lastly, the diffusion added here differs from the explicitly added so-called "artificial viscosity," commonly employed in computational models since its introduction by von Neumann and Richtmyer.[23] Traditional artificial viscosity has explicit dependence on the size of the discretization, and thus suffers similar defects as intrinsic numerical viscosity. While one might be tempted to classify the diffusion added in the present study as "artificial," one must realize that is distinct from typical artificial viscosity or numerical diffusion in that it is dependent on the physical scales rather than the discretization scales of the problem.

In the body of this paper, the extended BMSKS model will first be presented in a nominally conservative and then fully nonconservative form. After specification of common constitutive models, it will be impossible to express the governing equations in a fully conservative form. In an analysis similar to that for single phase materials, diffusion will be shown to be dissipative, and the entropy generation terms for each individual phase will be explicated. A simple set of fully conservative mixture equations is given with a rational set of mixture variables. In the one-dimensional limit, results from a standard characteristic analysis are presented which gives indication as to what conditions are necessary for a well posed problem in the presence of diffusion.

Numerical solutions are then presented to exercise the model. Because diffusion has been explicitly modeled, no exotic numerical methods are necessary; second order central differencing of spatial gradients has been applied to a nonconservative formulation of the equations to convert them to a large system of ordinary differential equations which are solved with a standard implicit time advancement scheme. In the limiting case of a mixture of two noninteracting ideal gases in a shock tube, the method is able to match well the results of an exact unsteady inviscid solution. Moreover, the solution is shown to be converging at a rate consistent with the method's order of accuracy. Next the unsteady model is shown to give predictions of the structure of viscous shocks in two noninteracting ideal gases which match well with the independent predictions of a steady Navier–Stokes model. Lastly, a series of problems with inert compaction waves in an interacting nonideal gas and solid HMX system is studied in such a way that the effects of intraphase diffusion, interphase compaction, momenta transfer, and energy transfer, as well as the irreversibility they induce, are quantified. At piston velocities sufficiently low so as to induce subsonic compaction waves, the effects of intraphase diffusion on compaction are small. At piston velocities sufficiently high to induce a coupled shock and compaction wave, intraphase diffusion

suppresses spurious oscillations predicted by a complementary inviscid model.

Simple constitutive models with parameters appropriate for typical heterogeneous energetic material are adopted. While these simple models may not be appropriate to match all known experimental observations, it has been shown[17] that similar approaches can properly capture correct orders of magnitude of most relevant phenomena. The models employed, including notably an interphase drag suggested by the experiments and analysis of Asay *et al.*,[24] demonstrate that for problems in which significant compaction occurs, interphase transport rapidly equilibrates solid and gas velocities and temperatures; compaction equilibrates solid pressures and configurational stress. Quantitative consideration of the dissipation in this problem shows conclusively that compaction is overwhelmingly dominant over all other interphase and intraphase mechanisms.

The novelty of this work lies in its (1) systematic extension of a two-phase reactive flow model to include diffusion of linear momenta and energy, (2) quantitative predictions of compaction wave phenomena using a solid equation of state with explicit volume fraction dependency in the manner first suggested by BMSKS, and (3) quantitative predictions of a budget of irreversibility generated by each mechanism, so that the relative importance of each can be gauged.

II. MODEL EQUATIONS

In this section, the extended BMSKS model is presented. Inasmuch as possible, an identical nomenclature is imposed.

A. Nominally conservative form

The nominally conservative form of the model equations is given here. Note that the later specification of the BMSKS constitutive theory will render this system to be inherently nonconservative.

$$\frac{\partial}{\partial t}(\rho_s \phi_s) + \boldsymbol{\nabla} \cdot (\rho_s \phi_s \mathbf{u}_s) = \mathcal{C}, \tag{1}$$

$$\frac{\partial}{\partial t}(\rho_g \phi_g) + \boldsymbol{\nabla} \cdot (\rho_g \phi_g \mathbf{u}_g) = -\mathcal{C}, \tag{2}$$

$$\frac{\partial}{\partial t}(\rho_s \phi_s \mathbf{u}_s) + \boldsymbol{\nabla} \cdot [\rho_s \phi_s \mathbf{u}_s \mathbf{u}_s^T + \phi_s(p_s \mathbf{I} - \boldsymbol{\tau}_s)] = \mathcal{M}, \tag{3}$$

$$\frac{\partial}{\partial t}(\rho_g \phi_g \mathbf{u}_g) + \boldsymbol{\nabla} \cdot [\rho_g \phi_g \mathbf{u}_g \mathbf{u}_g^T + \phi_g(p_g \mathbf{I} - \boldsymbol{\tau}_g)] = -\mathcal{M}, \tag{4}$$

$$\frac{\partial}{\partial t}\left[\rho_s \phi_s \left(e_s + \frac{1}{2}\mathbf{u}_s \cdot \mathbf{u}_s\right)\right] + \boldsymbol{\nabla} \cdot \left[\rho_s \phi_s \mathbf{u}_s \left(e_s + \frac{1}{2}\mathbf{u}_s \cdot \mathbf{u}_s\right)\right.$$
$$\left. + \phi_s \mathbf{u}_s \cdot (p_s \mathbf{I} - \boldsymbol{\tau}_s) + \phi_s \mathbf{q}_s\right] = \mathcal{E}, \tag{5}$$

$$\frac{\partial}{\partial t}\left[\rho_g \phi_g \left(e_g + \frac{1}{2}\mathbf{u}_g \cdot \mathbf{u}_g\right)\right] + \boldsymbol{\nabla} \cdot \left(\rho_g \phi_g \mathbf{u}_g \left(e_g + \frac{1}{2}\mathbf{u}_g \cdot \mathbf{u}_g\right)\right.$$
$$\left. + \phi_g \mathbf{u}_g \cdot (p_g \mathbf{I} - \boldsymbol{\tau}_g) + \phi_g \mathbf{q}_g\right) = -\mathcal{E}, \tag{6}$$

$$\frac{\partial \rho_s}{\partial t} + \nabla \cdot (\rho_s \mathbf{u}_s) = -\frac{\rho_s \mathcal{F}}{\phi_s}, \tag{7}$$

$$\frac{\partial}{\partial t}(\rho_s \phi_s \eta_s + \rho_g \phi_g \eta_g) + \nabla \cdot (\rho_s \phi_s \mathbf{u}_s \eta_s + \rho_g \phi_g \mathbf{u}_g \eta_g)$$

$$\geq -\nabla \cdot \left(\frac{\phi_s \mathbf{q}_s}{T_s} + \frac{\phi_g \mathbf{q}_g}{T_g} \right). \tag{8}$$

The subscripts s and g denote solid and gas phases, respectively; ρ, ϕ, $\mathbf{u}$, p, $\boldsymbol{\tau}$, e, $\mathbf{q}$, η, and T represent intrinsic densities, volume fractions, velocity vectors, pressures, viscous stress tensors, internal energies, heat flux vectors, entropies, and temperatures, respectively. The terms $\mathcal{C}$, $\mathcal{M}$, $\mathcal{E}$, and $\mathcal{F}$ represent interphase transport of mass, linear momenta, and energy, and a source term for material compaction, respectively. Equations (1)–(6) describe the evolution of mass, linear momenta, and energy in the solid and gas, respectively. Equation (7) is a relation modeling material compaction, widely used in the detonation community, albeit nontraditional. It is a useful *ad hoc* relation which allows volume fraction to evolve in response to interphase mass transfer as well as stress nonequilibrium. While lacking a rigorous justification based on averaging from the microstructural scale, it has proved able to (1) capture observed compaction phenomena,[6,7] (2) prevent initial and initial/boundary value problems from being ill posed in the sense of Hadamard, and (3) be useful in satisfying an entropy inequality. Equation (8) is the entropy inequality, extended for systems with intraphase energy diffusion. No consideration is given here to an angular momenta axiom; however, a complete theory for multidimensional motion, not studied here, will need to include this principle.

Equations (1)–(6) have been constructed to insure that whatever form the phase interaction terms $\mathcal{C}$, $\mathcal{M}$, and $\mathcal{E}$ take, appropriate mixture quantities are formally conserved. In fact, if the following mixture variables, denoted by the subscript m, and relative velocities, denoted by the subscript r are defined as

$$\rho_m \equiv \rho_s \phi_s + \rho_g \phi_g, \tag{9}$$

$$\mathbf{u}_m \equiv \frac{\rho_s \phi_s \mathbf{u}_s + \rho_g \phi_g \mathbf{u}_g}{\rho_s \phi_s + \rho_g \phi_g}, \tag{10}$$

$$\mathbf{u}_{rs} \equiv \mathbf{u}_s - \mathbf{u}_m, \tag{11}$$

$$\mathbf{u}_{rg} \equiv \mathbf{u}_g - \mathbf{u}_m, \tag{12}$$

$$p_m \equiv \phi_s(p_s + \tfrac{1}{3}\rho_s \mathbf{u}_{rs} \cdot \mathbf{u}_{rs}) + \phi_g(p_g + \tfrac{1}{3}\rho_g \mathbf{u}_{rg} \cdot \mathbf{u}_{rg}), \tag{13}$$

$$e_m \equiv \frac{\rho_s \phi_s \left(e_s + \dfrac{\mathbf{u}_{rs} \cdot \mathbf{u}_{rs}}{2} \right) + \rho_g \phi_g \left(e_g + \dfrac{\mathbf{u}_{rg} \cdot \mathbf{u}_{rg}}{2} \right)}{\rho_s \phi_s + \rho_g \phi_g}, \tag{14}$$

$$\boldsymbol{\tau}_m \equiv \phi_s \{ \boldsymbol{\tau}_s - \rho_s[\mathbf{u}_{rs}\mathbf{u}_{rs}^T - \tfrac{1}{3}(\mathbf{u}_{rs} \cdot \mathbf{u}_{rs})\mathbf{I}] \}$$

$$+ \phi_g \{ \boldsymbol{\tau}_g - \rho_g[\mathbf{u}_{rg}\mathbf{u}_{rg}^T - \tfrac{1}{3}(\mathbf{u}_{rg} \cdot \mathbf{u}_{rg})\mathbf{I}] \}, \tag{15}$$

$$\mathbf{q}_m \equiv \phi_s \left[\rho_s \mathbf{u}_{rs} \left(e_s + \frac{\mathbf{u}_{rs} \cdot \mathbf{u}_{rs}}{2} \right) + \mathbf{u}_{rs} \cdot (p_s \mathbf{I} - \boldsymbol{\tau}_s) + \mathbf{q}_s \right]$$

$$+ \phi_g \left[\rho_g \mathbf{u}_{rg} \left(e_g + \frac{\mathbf{u}_{rg} \cdot \mathbf{u}_{rg}}{2} \right) + \mathbf{u}_{rg} \cdot (p_g \mathbf{I} - \boldsymbol{\tau}_g) + \mathbf{q}_g \right], \tag{16}$$

then the sum of the mass, linear momenta, and energy evolution equations can be represented in a fully conservative form as

$$\frac{\partial \rho_m}{\partial t} + \nabla \cdot (\rho_m \mathbf{u}_m) = 0, \tag{17}$$

$$\frac{\partial}{\partial t}(\rho_m \mathbf{u}_m) + \nabla \cdot (\rho_m \mathbf{u}_m \mathbf{u}_m^T + p_m \mathbf{I} - \boldsymbol{\tau}_m) = 0, \tag{18}$$

$$\frac{\partial}{\partial t}\left[\rho_m \left(e_m + \frac{\mathbf{u}_m \cdot \mathbf{u}_m}{2} \right) \right] + \nabla \cdot \left[\rho_m \mathbf{u}_m \left(e_m + \frac{\mathbf{u}_m \cdot \mathbf{u}_m}{2} \right) \right.$$

$$\left. + \mathbf{u}_m \cdot (p_m \mathbf{I} - \boldsymbol{\tau}_m) + \mathbf{q}_m \right] = 0. \tag{19}$$

This is precisely the form of the classical compressible Navier–Stokes equations. While the derivation of the appropriate mixture and relative quantities given by Eqs. (9)–(16) is detailed, the results are easily verified by direct substitution into Eqs. (17)–(19) and comparison with the appropriate sums of evolution Eqs. (1)–(6). It is also seen that when the velocities of the components relative to that of the mixture are zero ($\mathbf{u}_{rs} = \mathbf{u}_{rg} = \mathbf{0}$), the mixture pressure, energy, shear stress, and heat flux reduce to simple mass- or volume-averages of the components. The relative velocities, analogous to fluctuation velocities of turbulence theory, induce corrections to pressure, energy, stress, and heat flux in an analogous fashion to Reynolds stresses in turbulence.

B. Constitutive equations

The system of Eqs. (1)–(7) is closed by specification of constitutive equations, designed in such a fashion to guarantee satisfaction of the entropy inequality, Eq. (8):

$$\phi_g + \phi_s = 1, \tag{20}$$

$$\psi_s = \hat{\psi}_s(\rho_s, T_s) + B(\phi_s), \tag{21}$$

$$\psi_g = \psi_g(\rho_g, T_g), \tag{22}$$

$$p_s = \rho_s^2 \left. \frac{\partial \psi_s}{\partial \rho_s} \right|_{T_s, \phi_s}, \tag{23}$$

$$p_g = \rho_g^2 \left. \frac{\partial \psi_g}{\partial \rho_g} \right|_{T_g}, \tag{24}$$

$$\eta_s = -\left. \frac{\partial \psi_s}{\partial T_s} \right|_{\rho_s, \phi_s}, \tag{25}$$

$$\eta_g = -\left. \frac{\partial \psi_g}{\partial T_g} \right|_{\rho_g}, \tag{26}$$

$$\beta_s = \rho_s \phi_s \left. \frac{\partial \psi_s}{\partial \phi_s} \right|_{\rho_s, T_s}, \tag{27}$$

$$e_s = \psi_s + T_s \eta_s, \tag{28}$$

$$e_g = \psi_g + T_g \eta_g, \tag{29}$$

$$\boldsymbol{\tau}_s = 2\mu_s \left(\frac{(\nabla \mathbf{u}_s)^T + \nabla \mathbf{u}_s}{2} - \frac{1}{3}(\nabla \cdot \mathbf{u}_s)\mathbf{I} \right), \tag{30}$$

$$\boldsymbol{\tau}_g = 2\mu_s \left(\frac{(\nabla \mathbf{u}_g)^T + \nabla \mathbf{u}_g}{2} - \frac{1}{3}(\nabla \cdot \mathbf{u}_g)\mathbf{I} \right), \tag{31}$$

$$\mathbf{q}_s = -k_s \nabla T_s, \tag{32}$$

$$\mathbf{q}_g = -k_g \nabla T_g, \tag{33}$$

$$\mathcal{C} = \mathcal{C}(\rho_s, \rho_g, T_s, T_g, \phi_s), \tag{34}$$

$$\mathcal{M} = p_g \nabla \phi_s - \delta(\mathbf{u}_s - \mathbf{u}_g) + \tfrac{1}{2}(\mathbf{u}_s + \mathbf{u}_g)\mathcal{C}, \tag{35}$$

$$\mathcal{E} = \mathcal{H}(T_g - T_s) - p_g \mathcal{F} + \mathbf{u}_s \cdot \mathcal{M} + \left(e_s - \frac{\mathbf{u}_s \cdot \mathbf{u}_s}{2} \right)\mathcal{C}, \tag{36}$$

$$\mathcal{F} = \frac{\phi_s \phi_g}{\mu_c}(p_s - \beta_s - p_g). \tag{37}$$

New variables in Eqs. (20)–(37) are ψ, the Helmholtz free energy and β_s, a configuration stress for the solid. The function $B(\phi_s)$ will be needed to account for the free energy associated with the configurational stress, while $\hat{\psi}_s$ accounts for the classical free energy of the solid. New parameters introduced are μ, a coefficient of viscosity, k, a coefficient of thermal conductivity, μ_c, a so-called compaction viscosity,

δ, an interphase drag parameter, and $\mathcal{H}$, an interphase heat transfer parameter. For simplicity, δ and $\mathcal{H}$ are taken here to be constants; it is common to allow both to have a dependency on the local state of the system.

Equation (20) requires that the mixture be saturated by solid and gas; the mixture contains no voids with vacuums. Equations (21) and (22) are canonical equations of state for the solid and gas, which will later be specified. Equations (23)–(29) are standard thermodynamic relations for pressure, entropy, and energy. Equations (30) and (31) are classical Newtonian relations between viscous stress and strain rate for an isotropic compressible material which satisfies Stokes' assumption. Equations (32) and (33) are Fourier's law for the solid and gas. Equation (27) is a definition of the configurational stress as detailed in BMSKS. Equations (34)–(37) are special forms of the interphase transport equations as reported in BMSKS, constructed to insure frame invariance and second law satisfaction. It is the term $p_g \nabla \phi_s$ in Eq. (35) which models nozzling and renders the system nonconservative.

As much of the analysis which will follow in later sections will be independent of the particular form of the thermodynamic state equations, the forms reported have been general. When numerical calculations are made later, specific state equations will be required, and they are reported here. Relatively simple choices are made which have been shown to accurately capture compaction and detonation wave speeds in heterogeneous energetic materials.[17]

BMSKS suggest a canonical form for state equations for granular materials, and application of their prescription to the Tait equation,[25] modified for compaction effects,[7] yields

$$\psi_s(\rho_s, T_s, \phi_s) = c_{vs} T_s \left[1 - \ln\left(\frac{T_s}{T_{s0}}\right) + (\gamma_s - 1)\ln\left(\frac{\rho_s}{\rho_{s0}}\right) \right] + \frac{1}{\gamma_s}\frac{\rho_{s0}}{\rho_s}\varepsilon_s + q$$
$$+ \frac{(p_{s0} - p_{g0})(2 - \phi_{s0})\ln\left[\frac{(1-\phi_{s0})^{2-\phi_{s0}}}{(1-\phi_s)^{2-\phi_s}} \left(\frac{2-\phi_s}{2-\phi_{s0}} \right)^{(2-\phi_s)(2-\phi_{s0})} \right]}{\rho_{s0}(2-\phi_s)\phi_{s0}\ln\left(\frac{1}{1-\phi_{s0}} \right)}. \tag{38}$$

Here c_{vs} is the constant specific heat at constant volume of the solid, γ_s is a constant related to the ratio of specific heats, ε_s is a constant with units of energy per mass fixed by matching to compaction wave speed data, ρ_{s0} and T_{s0} are the reference density and temperature for the solid, p_{s0} and p_{g0} are reference solid and gas pressures, which are calculated such that they are consistent with the reference states for density and temperature, ϕ_{s0} is the ambient solid volume fraction, and q is the chemical energy of the solid. Applying Eqs. (23), (25), (28), and (27) to the canonical form (38) yields

$$p_s = (\gamma_s - 1)c_{vs}\rho_s T_s - \frac{1}{\gamma_s}\rho_{s0}\varepsilon_s, \tag{39}$$

$$\eta_s = c_{vs}\ln\left(\frac{T_s}{T_{s0}}\right) - (\gamma_s - 1)c_{vs}\ln\left(\frac{\rho_s}{\rho_{s0}}\right), \tag{40}$$

$$e_s = c_{vs}T_s + \frac{1}{\gamma_s}\frac{\rho_{s0}}{\rho_s}\varepsilon_s + q + \frac{(p_{s0} - p_{g0})(2 - \phi_{s0})\ln\left[\frac{(1-\phi_{s0})^{2-\phi_{s0}}}{(1-\phi_s)^{2-\phi_s}} \left(\frac{2-\phi_s}{2-\phi_{s0}} \right)^{(2-\phi_s)(2-\phi_{s0})} \right]}{\rho_{s0}(2-\phi_s)\phi_{s0}\ln\left(\frac{1}{1-\phi_{s0}} \right)}, \tag{41}$$

$$\beta_s = (p_{s0} - p_{g0}) \frac{\rho_s \phi_s}{\rho_{s0} \phi_{s0}} \left(\frac{2 - \phi_{s0}}{2 - \phi_s} \right)^2 \frac{\ln\left(\frac{1}{1 - \phi_s} \right)}{\ln\left(\frac{1}{1 - \phi_{s0}} \right)}. \tag{42}$$

For the gas, a virial equation of state is adopted, which has canonical form

$$\psi_g(\rho_g, T_g) = c_{vg} T_g \left\{ 1 - \ln\left(\frac{T_g}{T_{g0}} \right) + (\gamma_g - 1) \left[\ln\left(\frac{\rho_g}{\rho_{g0}} \right) \right. \right.$$
$$\left. \left. + b_g(\rho_g - \rho_{g0}) \right] \right\}. \tag{43}$$

Here c_{vg} is the constant specific heat at constant volume of the gas, γ_g is a constant related to the ratio of specific heats, b_g is the virial coefficient, and T_{g0} and ρ_{g0} are reference states for the gas. Applying Eqs. (24), (26), and (29) to the canonical form (43) yields

$$p_g = (\gamma_g - 1) c_{vg} \rho_g T_g (1 + b_g \rho_g), \tag{44}$$

$$\eta_g = c_{vg} \ln\left(\frac{T_g}{T_{g0}} \right) - (\gamma_g - 1) c_{vg} \left[\ln\left(\frac{\rho_g}{\rho_{g0}} \right) + b(\rho_g - \rho_{g0}) \right], \tag{45}$$

$$e_g = c_{vg} T_g. \tag{46}$$

C. Fully nonconservative form

A detailed analysis of the type given by Powers *et al.*[8] and BMSKS allows Eqs. (1)–(8) to be written in a fully nonconservative form. This analysis involves systematic elimination of terms involving mass and linear momenta from the energy equations, and elimination of terms involving mass from the linear momenta equations. Doing this as well as (1) directly invoking constitutive models for interphase momenta and energy transport and compaction (35)–(37), and (2) defining material derivatives for the solid and gas, respectively, as $d/dt_s \equiv \partial/\partial t + \mathbf{u}_s \cdot \nabla$, $d/dt_g \equiv \partial/\partial t + \mathbf{u}_g \cdot \nabla$, one obtains

$$\frac{d\rho_s}{dt_s} = -\rho_s \nabla \cdot \mathbf{u}_s - \frac{\rho_s \mathcal{F}}{\phi_s}, \tag{47}$$

$$\frac{d\rho_g}{dt_g} = -\rho_g \nabla \cdot \mathbf{u}_g + \frac{\mathcal{C}}{\phi_g}\left(\frac{\rho_g}{\rho_s} - 1 \right)$$
$$+ \frac{\rho_g \mathcal{F}}{\phi_g} + \frac{\rho_g}{\phi_g}(\mathbf{u}_s - \mathbf{u}_g) \cdot \nabla \phi_g, \tag{48}$$

$$\rho_s \phi_s \frac{d\mathbf{u}_s}{dt_s} = -\phi_s \nabla p_s + (p_g - p_s) \nabla \phi_s + \phi_s \nabla \cdot \boldsymbol{\tau}_s + \boldsymbol{\tau}_s \cdot \nabla \phi_s$$
$$- \delta(\mathbf{u}_s - \mathbf{u}_g) + \tfrac{1}{2}(\mathbf{u}_g - \mathbf{u}_s)\mathcal{C}, \tag{49}$$

$$\rho_g \phi_g \frac{d\mathbf{u}_g}{dt_g} = -\phi_g \nabla p_g + \phi_g \nabla \cdot \boldsymbol{\tau}_g + \boldsymbol{\tau}_g \cdot \nabla \phi_g + \delta(\mathbf{u}_s - \mathbf{u}_g)$$
$$+ \tfrac{1}{2}(\mathbf{u}_g - \mathbf{u}_s)\mathcal{C}, \tag{50}$$

$$\rho_s \phi_s \frac{de_s}{dt_s} = -p_s \phi_s \nabla \cdot \mathbf{u}_s + \phi_s \boldsymbol{\tau}_s : \nabla \mathbf{u}_s - p_g \mathcal{F} + \mathcal{H}(T_g - T_s)$$
$$- \phi_s \nabla \cdot \mathbf{q}_s - \mathbf{q}_s \cdot \nabla \phi_s, \tag{51}$$

$$\rho_g \phi_g \frac{de_g}{dt_g} = -p_g \phi_g \nabla \cdot \mathbf{u}_g + p_g(\mathbf{u}_s - \mathbf{u}_g) \cdot \nabla \phi_g + \phi_g \boldsymbol{\tau}_g : \nabla \mathbf{u}_g$$
$$+ p_g \mathcal{F} - \mathcal{H}(T_g - T_s) - \phi_g \nabla \cdot \mathbf{q}_g - \mathbf{q}_g \cdot \nabla \phi_g$$
$$+ \delta(\mathbf{u}_s - \mathbf{u}_g) \cdot (\mathbf{u}_s - \mathbf{u}_g) - (e_s - e_g)\mathcal{C}, \tag{52}$$

$$\frac{d\phi_s}{dt_s} = \mathcal{F} + \frac{\mathcal{C}}{\rho_s}, \tag{53}$$

$$\rho_s \phi_s \frac{d\eta_s}{dt_s} + \rho_g \phi_g \frac{d\eta_g}{dt_g} + \mathcal{C}(\eta_s - \eta_g)$$
$$\geq -\frac{\phi_s}{T_s} \nabla \cdot \mathbf{q}_s + \frac{\phi_s}{T_s^2} \mathbf{q}_s \cdot \nabla T_s - \frac{1}{T_s} \mathbf{q}_s \cdot \nabla \phi_s$$
$$- \frac{\phi_g}{T_g} \nabla \cdot \mathbf{q}_g + \frac{\phi_g}{T_g^2} \mathbf{q}_g \cdot \nabla T_g - \frac{1}{T_g} \mathbf{q}_g \cdot \nabla \phi_g. \tag{54}$$

It is noted that in this fully nonconservative form, velocities only appear as differences; consequently, it is easy to show that the equations are invariant under a Galilean change of reference frame.

D. Dissipation

It is now possible to determine what conditions are necessary for Eqs. (47)–(53) to satisfy the second law (54). First one must consider the rate of entropy change in each phase. To do this, first consider thermodynamic Gibbs identities

$$T_s \frac{d\eta_s}{dt_s} = \frac{de_s}{dt_s} - \frac{p_s}{\rho_s^2} \frac{d\rho_s}{dt_s} - \frac{\beta_s}{\rho_s \phi_s} \frac{d\phi_s}{dt_s}, \tag{55}$$

$$T_g \frac{d\eta_g}{dt_g} = \frac{de_g}{dt_g} - \frac{p_g}{\rho_g^2} \frac{d\rho_g}{dt_g}, \tag{56}$$

consequences of Eqs. (22)–(29) and (27), developed in full by BMSKS. Next use Eqs. (55) and (56) to eliminate energy derivatives in favor of entropy derivatives in Eqs. (51) and (52) to get alternate expressions for the first law of thermodynamics for the solid and gas:

$$\rho_s \phi_s T_s \frac{d\eta_s}{dt_s} = \mathcal{H}(T_g - T_s) - \phi_s \boldsymbol{\nabla} \cdot \mathbf{q}_s - \mathbf{q}_s \cdot \boldsymbol{\nabla} \phi_s$$

$$+ \phi_s \boldsymbol{\tau}_s : \boldsymbol{\nabla} \mathbf{u}_s + \frac{\phi_s \phi_g}{\mu_c} (p_s - \beta_s - p_g)^2$$

$$+ \beta_s \frac{(-\mathcal{C})}{\rho_s}, \tag{57}$$

$$\rho_g \phi_g T_g \frac{d\eta_g}{dt_g} = -\mathcal{H}(T_g - T_s) - \phi_g \boldsymbol{\nabla} \cdot \mathbf{q}_g - \mathbf{q}_g \cdot \boldsymbol{\nabla} \phi_g$$

$$+ \phi_g \boldsymbol{\tau}_g : \boldsymbol{\nabla} \mathbf{u}_g + \delta (\mathbf{u}_s - \mathbf{u}_g) \cdot (\mathbf{u}_s - \mathbf{u}_g)$$

$$+ \left[e_s - e_g - p_g \left(\frac{1}{\rho_g} - \frac{1}{\rho_s} \right) \right] (-\mathcal{C}). \tag{58}$$

It is obvious from Eq. (57) that terms related to material compaction, those involving μ_c, are inducing positive semidefinite changes in the solid entropy only. It is also obvious that interphase drag is inducing positive semidefinite changes in the gas entropy only. The BMSKS model has additional degrees of freedom to partition this dissipation among the phases, though they give arguments for recommending these choices. One also notes that the entropy of an individual phase can rise or fall in response to general interphase and intraphase transport; the second law only provides restrictions when the entire mixture is considered.

Substitution of the modified energy Eqs. (57) and (58) into the second law (54) yields, after simplification,

$$\frac{1}{T_s} \left[\mathcal{H}(T_g - T_s) - \frac{\phi_s}{T_s} \mathbf{q}_s \cdot \boldsymbol{\nabla} T_s + \phi_s \boldsymbol{\tau}_s : \boldsymbol{\nabla} \mathbf{u}_s \right.$$

$$+ \frac{\phi_s \phi_g}{\mu_c} (p_s - \beta_s - p_g)^2 + \beta_s \frac{(-\mathcal{C})}{\rho_s} \left. \right] + \frac{1}{T_g} \left\{ -\mathcal{H}(T_g - T_s) \right.$$

$$- \frac{\phi_g}{T_g} \mathbf{q}_g \cdot \boldsymbol{\nabla} T_g + \phi_g \boldsymbol{\tau}_g : \boldsymbol{\nabla} \mathbf{u}_g + \delta (\mathbf{u}_s - \mathbf{u}_g) \cdot (\mathbf{u}_s - \mathbf{u}_g)$$

$$+ \left[e_s - e_g - p_g \left(\frac{1}{\rho_g} - \frac{1}{\rho_s} \right) \right] (-\mathcal{C}) \left. \right\} + (-\mathcal{C})(\eta_g - \eta_s) \geq 0. \tag{59}$$

Now consider entropy changes induced by intraphase momenta diffusion. First define the standard viscous dissipation functions Φ as

$$\Phi_s = \boldsymbol{\tau}_s : \boldsymbol{\nabla} \mathbf{u}_s, \quad \Phi_g = \boldsymbol{\tau}_g : \boldsymbol{\nabla} \mathbf{u}_g. \tag{60}$$

By employing the Newtonian assumption (30) and (31), after some effort involving the use of quadratic forms, the viscous dissipation functions can be cast in a positive semidefinite form involving the squares of the portions of the strain rates that deviate from the mean strain rates.

$$\Phi_s = 2\mu_s \left(\underbrace{\underbrace{\frac{\boldsymbol{\nabla} \mathbf{u}_s + (\boldsymbol{\nabla} \mathbf{u}_s)^T}{2}}_{\text{strain rate}} - \underbrace{\frac{1}{3}(\boldsymbol{\nabla} \cdot \mathbf{u}_s)\ \mathbf{I}}_{\text{mean strain rate}}}_{\text{deviatoric strain rate}} \right) : \left(\underbrace{\underbrace{\frac{\boldsymbol{\nabla} \mathbf{u}_s + (\boldsymbol{\nabla} \mathbf{u}_s)^T}{2}}_{\text{strain rate}} - \underbrace{\frac{1}{3}(\boldsymbol{\nabla} \cdot \mathbf{u}_s)\ \mathbf{I}}_{\text{mean strain rate}}}_{\text{deviatoric strain rate}} \right), \tag{61}$$

$$\Phi_g = 2\mu_g \left(\underbrace{\underbrace{\frac{\boldsymbol{\nabla} \mathbf{u}_g + (\boldsymbol{\nabla} \mathbf{u}_g)^T}{2}}_{\text{strain rate}} - \underbrace{\frac{1}{3}(\boldsymbol{\nabla} \cdot \mathbf{u}_g)\ \mathbf{I}}_{\text{mean strain rate}}}_{\text{deviatoric strain rate}} \right) : \left(\underbrace{\underbrace{\frac{\boldsymbol{\nabla} \mathbf{u}_g + (\boldsymbol{\nabla} \mathbf{u}_g)^T}{2}}_{\text{strain rate}} - \underbrace{\frac{1}{3}(\boldsymbol{\nabla} \cdot \mathbf{u}_g)\ \mathbf{I}}_{\text{mean strain rate}}}_{\text{deviatoric strain rate}} \right). \tag{62}$$

Because the materials have been chosen to be Newtonian, which implies the viscous stress varies linearly with the strain rate, and satisfy Stokes' assumption, which implies the mean total stress is equal to the thermodynamic stress, certain consequences arise. First, it can be shown that the viscous stress is entirely deviatoric, and that it is induced only by deviatoric strain rates. Moreover, the viscous dissipation is induced only by deviatoric strain rates. The deviatoric strain rates are volume preserving. Mean strain rates are equivalent to volumetric deformations and here are associated entirely with mean stresses, in this case the thermodynamic stresses p_s and p_g. As here the mean stresses and mean strain rates do not induce entropy changes while doing work, it is concluded they induce only reversible energy changes.

Substituting Eqs. (61) and (62) as well as Eqs. (32) and (33) into Eq. (59) and rearranging, one finds a result equivalent to that of BMSKS for the extended system:

$$I \equiv (-\mathcal{C}) \left(\frac{\beta_s}{\rho_s T_s} + \frac{e_s - e_g - p_g(1/\rho_g - 1/\rho_s)}{T_g} + \eta_g - \eta_s \right)$$

$$+ \delta \frac{(\mathbf{u}_s - \mathbf{u}_g) \cdot (\mathbf{u}_s - \mathbf{u}_g)}{T_g} + \mathcal{H} \frac{(T_g - T_s)^2}{T_g T_s}$$

$$+ \frac{\phi_s \phi_g}{\mu_c} \frac{(p_s - \beta_s - p_g)^2}{T_s} + \frac{\phi_s \Phi_s}{T_s} + \frac{\phi_g \Phi_g}{T_g}$$

$$+ \frac{k_s \phi_s \boldsymbol{\nabla} T_s \cdot \boldsymbol{\nabla} T_s}{T_s^2} + \frac{k_g \phi_g \boldsymbol{\nabla} T_g \cdot \boldsymbol{\nabla} T_g}{T_g^2} \geq 0. \tag{63}$$

Here the irreversibility production rate I has been defined. With this form, it is easy to see how each transport mechanism contributes to the irreversibility, which enables one to make a quantitative calculation of the relative importance of each mechanism. The so-called strong form of the second law is satisfied provided each term in Eq. (63) is positive semidefinite, thus requiring $\mathcal{C} \leq 0$, $\delta \geq 0$, $\mathcal{H} \geq 0$, $\mu_c \geq 0$, $\mu_s \geq 0$, $\mu_g \geq 0$, $k_s \geq 0$, $k_g \geq 0$, and

$$\frac{e_g - e_s + p_g(1/\rho_g - 1/\rho_s)}{T_g} \leq \frac{\beta_s}{\rho_s T_s} + \eta_g - \eta_s. \tag{64}$$

BMSKS provide a plausible argument why the final nonclassical condition is likely to be satisfied.

E. Characteristics

In order to determine what boundary conditions are necessary to constitute a well posed problem, it is helpful to consider a characteristic analysis of the unsteady system in the one-dimensional limit. As discussed by Drew and Passman,[26] the issue of well-posedness for general two-phase systems remains controversial. Common inviscid systems without dynamic compaction equations such as Eq. (7) are known to be ill posed for initial value problems. And as discussed in recent work by Kreiss and Yström,[27] the common technique of relying on diffusion, numerical or physical, to stabilize models which are ill posed in the zero diffusion limit is questionable.

In the one-dimensional limit, with x as the spatial coordinate, Eqs. (47)–(53) coupled with constitutive Eqs. (20)–(37) can be cast as a system of first order partial differential equations of the form

$$\mathbf{A} \cdot \frac{\partial \mathbf{w}}{\partial t} + \mathbf{B} \cdot \frac{\partial \mathbf{w}}{\partial x} = \mathbf{c}. \tag{65}$$

Here $\mathbf{w}$ is a vector of length n containing the dependent variables, $\mathbf{c}$ is a vector of length n, and $\mathbf{A}$ and $\mathbf{B}$ are $n \times n$ matrices all of which are functions of x, t, and $\mathbf{w}$. In a standard analysis, such as that described by Zauderer,[28] one seeks curves in x-t space described by $dx/dt = \lambda$ along which Eq. (65) can be cast as ordinary differential equations. In so doing, one is led to the generalized eigenvalue problem

$$\mathbf{g} \cdot (\lambda \mathbf{A} - \mathbf{B}) = \mathbf{0}, \tag{66}$$

where $\mathbf{g}$ is a generalized eigenvector, and λ, often called a characteristic, is a generalized eigenvalue. The characteristics are found by satisfying the condition

$$|\lambda \mathbf{A} - \mathbf{B}| = 0. \tag{67}$$

The system is defined as hyperbolic if all generalized eigenvalues are real and n linearly independent generalized eigenvectors can be identified. If all the generalized eigenvalues are real and there are fewer than n linearly independent generalized eigenvectors, the system is defined as parabolic. If all of the generalized eigenvalues are complex, the system is elliptic. If some are real and some are complex, the system is of mixed type, and has some of the features of elliptic systems. Deciding how to formulate problems which are well posed in the sense of Hadamard is in general difficult. As a rule of thumb, hyperbolic systems are well posed when initial values are provided on a curve which is not a characteristic curve of the system. This constitutes an initial value problem. Parabolic problems typically require initial data; these are supplemented with boundary value data to constitute an initial and boundary value problem. Elliptic problems typically do not evolve in time; conditions are required at all geometrical boundaries to constitute a well posed boundary value problem.

1. No diffusion

In the limit of zero diffusion, $\mu_g = \mu_s = 0$, $k_g = k_s = 0$, it is well known that the system (47)–(53) is hyperbolic. In a calculation first reported for this class of systems by Baer and Nunziato,[5] the dimension of the system is $n = 7$, and it is found that

$$\lambda = u_s, u_s, u_s \pm c_s, u_g, u_g \pm c_g. \tag{68}$$

Here c_s and c_g are the isentropic sound speeds of the solid and gas, respectively, defined by

$$c_s = \sqrt{\left. \frac{\partial p_s}{\partial \rho_s} \right|_{\eta_s, \phi_s}}, \quad c_g = \sqrt{\left. \frac{\partial p_g}{\partial \rho_g} \right|_{\eta_g}}. \tag{69}$$

The seven generalized eigenvalues are real, though only six are distinct. However, it is easy to show that there are seven linearly independent generalized eigenvectors; hence, the full system can be projected onto these vectors, and the full system is hyperbolic, and thus well posed for initial value problems.

2. Energy diffusion

Consideration of energy but not momentum diffusion, while perhaps not physically important, yields a result with an interesting interpretation. Inclusion of Fourier heat conduction here raises the dimension of the system to $n = 9$. After a detailed analysis involving standard thermodynamic derivative manipulations, the generalized eigenvalues are found to be

$$\lambda = \begin{cases} u_s, \\[2ex] u_s \pm \sqrt{\left. \frac{\partial p_s}{\partial \rho_s} \right|_{T_s, \phi_s} + \left. \frac{\partial p_s}{\partial T_s} \right|_{\rho_s, \phi_s} \left(\frac{T_s}{\rho_s^2 c_{vs}} \left. \frac{\partial p_s}{\partial T_s} \right|_{\rho_s, \phi_s} - \left. \frac{\partial T_s}{\partial \rho_s} \right|_{\eta_s, \phi_s} \right)}, \\[3ex] u_g \pm \sqrt{\left. \frac{\partial p_g}{\partial \rho_g} \right|_{T_g} + \left. \frac{\partial p_g}{\partial T_g} \right|_{\rho_g} \left(\frac{T_g}{\rho_g^2 c_{vg}} \left. \frac{\partial p_g}{\partial T_g} \right|_{\rho_g} - \left. \frac{\partial T_g}{\partial \rho_g} \right|_{\eta_g} \right)}. \end{cases} \tag{70}$$

Here, there are five generalized eigenvalues, and they are all real and distinct. In the limit of two calorically perfect ideal gases, these equations simplify considerably to form $\lambda = u_s, u_s \pm c_s^T, u_g \pm c_g^T$, where c_s^T and c_g^T are the so-called iso-thermal sound speeds, $c_s^T \equiv \partial p_s / \partial \rho_s |_{T_s, \phi_s}$, $c_g^T \equiv \partial p_g / \partial \rho_g |_{T_g}$. Consequently in this limit, Newton's isothermal theory to predict acoustic propagation speeds is correct, though never realized in practice.

In this case while five generalized eigenvectors **g** can be found for each of the five generalized eigenvalues, there are not enough generalized eigenvectors to transform the entire system into characteristic form. Thus the system is parabolic, and it appears reasonable to assume that should appropriate Dirichlet, Neumann, or Robin boundary conditions on T_s and T_g be provided, the initial and boundary value problem is well posed. Thus with four boundary conditions (two at each end of the one dimensional domain) on temperature and five initial conditions on other variables, there are enough conditions for the nine equations.

3. Momentum and energy diffusion

Consideration of simultaneous energy and momentum diffusion is more typical in nature, especially in gas systems. Inclusion of Fourier heat conduction and viscous stresses here raises the dimension of the system to $n=11$. Another detailed but straightforward calculation reveals that the generalized eigenvalues are simply

$$\lambda = u_s, u_s, u_g. \tag{71}$$

For each of the three generalized eigenvalues, of which two are indistinct, three generalized eigenvectors **g** can be found. Once again, there are not enough generalized eigenvectors to transform the entire system into characteristic form. Thus the system is not hyperbolic; it is, however, parabolic, and should appropriate Dirichlet, Neumann, or Robin boundary conditions on T_s, T_g, u_s, and u_g be provided, it is reasonable to suppose that the initial and boundary value problem is well posed. Thus with eight boundary conditions (four at each end) on T_s, T_g, u_s, and u_g and three initial conditions on other variables, there are enough conditions for the eleven equations.

III. NUMERICAL METHOD

The one-dimensional form of Eqs. (47)–(53) is solved with a straightforward numerical technique. Because thin, but finite, diffusion layers in shocks have been explicitly modeled and will be fully resolved, there is no compelling need to resort to more complicated numerical schemes. Solutions are considered on the domain $x \in [0, L]$, $t \in [0, \infty)$, where L is the domain length. A set of N points is uniformly distributed on the domain, where all variables, with the exception of heat fluxes and viscous stresses, will take their values. Heat fluxes and viscous stresses are assigned values halfway between each of the N points. Next the spatial gradient operators in Eqs. (47)–(53) are approximated by a central difference scheme of second order spatial accuracy. Only boundaries at $x=0$ and $x=L$ which are no-slip and adiabatic are considered, and so, consistent with the detailed discus-

sion of Poinsot and Lele,[29] it is required that the following eight boundary conditions be satisfied:

$$u_g(0,t) = u_g(L,t) = u_s(0,t) = u_s(L,t) = 0, \tag{72}$$

$$q_g(0,t) = q_g(L,t) = q_s(0,t) = q_s(L,t) = 0. \tag{73}$$

At these boundaries, second order one-sided difference schemes are employed to maintain the overall accuracy of the method. Appropriate extrapolation techniques are used to account for the fact that heat fluxes and viscous stresses are defined at the midpoints of the primary grid.

At this point the system is represented by a large system of coupled nonlinear ordinary differential equations. These are then solved with an implicit Adams method as embodied in the widely available Fortran code, DLSODE.[30] This code provides automatic time step selection prescribed in such a manner to achieve a user-defined error tolerance. This error tolerance was set well below the level of truncation error for the spatial discretization.

All calculations were done using a FORTRAN90 code running on a Macintosh PowerBook G4 laptop computer operating at 667 MHz. Depending on the numerical stiffness of the source terms, calculations for $N=1001$ grid points required anywhere from 5 min to 1 h. The longest calculation on a highly refined $N=10\,001$ grid took approximately 7 h.

IV. VERIFICATION OF NUMERICAL METHOD

Two cases were calculated for which known benchmark solutions existed in order to verify the numerical method: a shock tube and a piston-driven shock. Intraphase diffusion was present in all cases, with coefficients selected so that the viscous zone enveloped several grain diameters, and so that the Prandtl number, $Pr = \gamma \mu c_v / k$, for both solid and gas was of order unity, thus rendering momentum and energy diffusion to be of similar importance. To achieve this end, values for μ and k are significantly higher than they are for single phase materials, and thus this simple model cannot at the same time describe ordinary slow macroscale diffusion. For problems such as cookoff where slow diffusion is important, a more sophisticated constitutive theory could be employed in which the diffusion coefficients had strain-rate dependency.

A. Case A: Shock tube

In the classical shock tube problem, two halves of the domain are held at the same temperature, with the left side held initially at an elevated density, given by $\hat{\rho}_{s0}$ and $\hat{\rho}_{g0}$, and consequent pressures. At $t=0$, the system is set into motion, and a shock propagates to the right, a material discontinuity to the left, and a rarefaction to the left. In the limit of a single inviscid calorically perfect ideal gas, a closed form analytic solution is known, as given, for example, by Shapiro.[31]

Using parameters of Table I, the motion of two viscous uncoupled calorically perfect ideal gases propagating at different speeds in a shock tube is calculated. In this simulation all interphase transport is suppressed. In order to keep the

TABLE I. Parameter values for (A) shock tube, (B) simple piston, (C) piston with subsonic compaction, (D) piston with subsonic compaction and drag, (E) piston with subsonic compaction, drag, and heat transfer, and (F) piston with supersonic compaction, drag, and heat transfer.

Parameter	Units	Case A	Case B	Case C	Case D	Case E	Case F
t_{max}	s	6×10^{-5}	1.2×10^{-4}	6×10^{-4}	6×10^{-4}	6×10^{-4}	1×10^{-5}
N	$\cdots$	1001	1001	1001	1001	1001	5001
L	m	5×10^{-1}	5×10^{-1}	5×10^{-1}	5×10^{-1}	5×10^{-1}	5×10^{-1}
Δx	m	5×10^{-4}	5×10^{-4}	5×10^{-4}	5×10^{-4}	5×10^{-4}	1×10^{-4}
u_p^{max}	m/s	0	1×10^2	1×10^2	1×10^2	1×10^2	1×10^3
t_{rise}	s	0	1×10^{-6}	1×10^{-6}	1×10^{-6}	1×10^{-6}	1×10^{-6}
μ_g	N s/m^2	1×10^0	1×10^0	1×10^0	1×10^0	1×10^0	$1\times10^0\|0$
μ_s	N s/m^2	1×10^3	1×10^3	1×10^3	1×10^3	1×10^3	$1\times10^3\|0$
k_g	W/m/K	1×10^3	1×10^3	1×10^3	1×10^3	1×10^3	$1\times10^3 \| 0$
k_s	W/m/K	1×10^6	1×10^6	1×10^6	1×10^6	1×10^6	$1\times10^6\|0$
μ_c	N s/m^2	∞	∞	1×10^3	1×10^3	1×10^3	1×10^3
δ	kg/m^3/s	0	0	0	1×10^8	1×10^8	1×10^8
$\mathcal{H}$	W/m^3/K	0	0	0	0	1×10^{10}	1×10^{10}
$\mathcal{C}$	kg/m^3/s	0	0	0	0	0	0
q	J/kg	0	0	0	0	0	0
γ_g	$\cdots$	2.70×10^0	2.70×10^0	1.35×10^0	1.35×10^0	1.35×10^0	1.35×10^0
c_{vg}	J/kg/K	2.4×10^3	2.4×10^3	2.4×10^3	2.4×10^3	2.4×10^3	2.4×10^3
b_g	m^3/kg	0	0	1.1×10^{-3}	1.1×10^{-3}	1.1×10^{-3}	1.1×10^{-3}
T_{g0}	K	3×10^2	3×10^2	3×10^2	3×10^2	3×10^2	3×10^2
T_{s0}	K	3×10^2	3×10^2	3×10^2	3×10^2	3×10^2	3×10^2
ρ_{g0}	kg/m^3	1×10^0	1×10^0	1×10^0	1×10^0	1×10^0	1×10^0
$\hat{\rho}_{g0}$	kg/m^3	1.1×10^0	1×10^0	1×10^0	1×10^0	1×10^0	1×10^0
γ_s	$\cdots$	5×10^0	5×10^0	5×10^0	5×10^0	5×10^0	5×10^0
ε_s	J/kg	0	0	8.98×10^6	8.98×10^6	8.98×10^6	8.98×10^6
c_{vs}	J/kg/K	1.5×10^3	1.5×10^3	1.5×10^3	1.5×10^3	1.5×10^3	1.5×10^3
ρ_{s0}	kg/m^3	1.9×10^3	1.9×10^3	1.9×10^3	1.9×10^3	1.9×10^3	1.9×10^3
$\hat{\rho}_{s0}$	kg/m^3	2.0×10^3	1.9×10^3	1.9×10^3	1.9×10^3	1.9×10^3	1.9×10^3
ϕ_{s0}	$\cdots$	7.3×10^{-1}	7.3×10^{-1}	7.3×10^{-1}	7.3×10^{-1}	7.3×10^{-1}	7.3×10^{-1}

waves relatively close to one another for a good comparison, the parameter γ_g has been set to a higher value, $\gamma_g=2.70$, than is typical for gases. For compaction wave studies, its value is returned to a more typical $\gamma_g=1.35$.

In Fig. 1, part A1, predictions of temperature at a final time $t_{max}=60$ μs are shown along with the predictions of the inviscid theory. The agreement is remarkably good, with the main difference being that the viscous model predicts waves with finite thickness, due to physical diffusion. No phenomena typically associated with numerical noise, such as Gibbs phenomena or dispersion effects are seen at these scales, primarily because the physical diffusion is of a sufficiently high magnitude to render them indistinguishable. As the method is formally not flux conservative, there is a very small evolution of total mass and total energy in the system, which can be made as small as one likes with grid refinement.

In Fig. 1, part A2, predictions of how an error norm for temperature behaves as the grid is refined is given. Here a 1-normed error L_1 is defined as representative of the average error of the combination of the solid and gas temperature:

$$L_1=\frac{1}{2N}\sum_{i=1}^{N}\left(|T_{si}-T_{si}^e|+|T_{gi}-T_{gi}^e|\right). \tag{74}$$

Here T_{si} and T_{gi} are the approximations for the solid and gas temperatures at the ith grid point, and T_{si}^e and T_{gi}^e are the values of the exact solution at the corresponding grid points. The exact solution is estimated from a highly refined solution
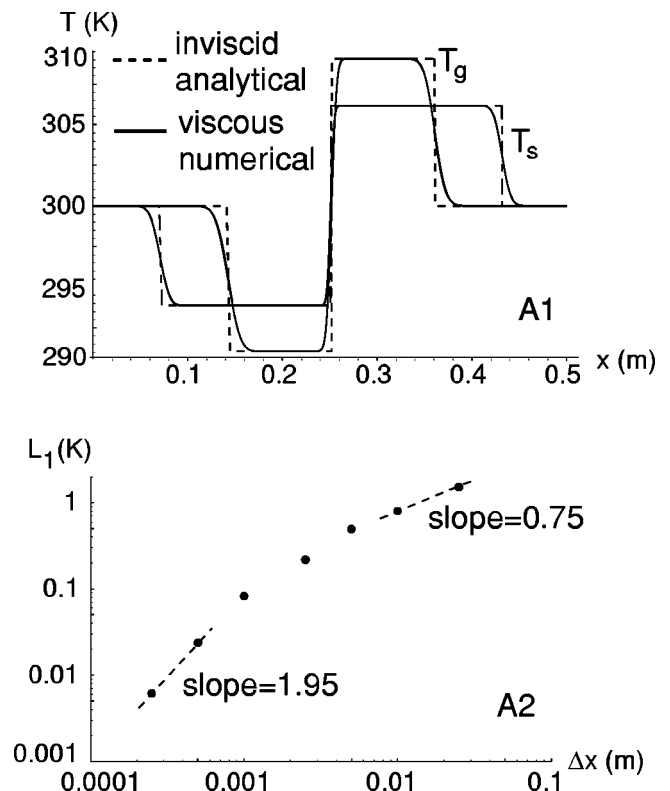

FIG. 1. Results for case A. (A1) Analytic (dotted lines) and computational (solid lines) solutions for the shock tube problem, (A2) behavior of error norm of temperature as the grid is refined.

with $N=10\,001$. Figure 1, part A2, clearly shows that L_1 is converging to zero. For very coarse grids, the convergence rate is $O(\Delta x^{0.75})$, while for fine grids, the convergence rate is $O(\Delta x^{1.95})$, which is approaching the order of the inherent truncation error of the second order discretization. Examination of the solution at coarse resolution shows many effects of numerical noise dominating the unresolved physical diffusion; numerical artifacts become unrecognizable when the grid is refined such that the physical viscous layers are resolved.

B. Case B: Piston-driven shocks

In case B, a simulation of a piston driving into two non-interacting calorically perfect viscous ideal gases is presented. In this case, the motion of a piston, located at $x=0$ when $t=0$, and having velocity u_p of

$$u_p(t)=u_p^{max}\left[1-\exp\left(-\frac{t}{t_{rise}}\right)\right],\tag{75}$$

is modeled. Here u_p^{max} is the maximum piston velocity, and t_{rise} is the rise time for the piston acceleration, here set to be $t_{rise}=1\,\mu s$. To achieve this effect, Eqs. (47)–(53) were subjected to an appropriate transformation to the accelerating reference frame in which the transformed velocity at the piston face was zero. This is achieved by effecting

$$\tilde{x}=x-u_p^{max}\left\{t+t_{rise}\left[\exp\left(-\frac{t}{t_{rise}}\right)-1\right]\right\},\tag{76}$$

$$\tilde{t}=t.\tag{77}$$

The velocities and accelerations in the accelerating frame are then given by

$$\tilde{u}_s=u_s-u_p^{max}\left[1-\exp\left(-\frac{t}{t_{rise}}\right)\right],\tag{78}$$

$$\tilde{u}_g=u_g-u_p^{max}\left[1-\exp\left(-\frac{t}{t_{rise}}\right)\right],\tag{79}$$

$$\frac{d\tilde{u}_s}{d\tilde{t}_s}=\frac{du_s}{dt_s}-\frac{u_p^{max}}{t_{rise}}\exp\left(-\frac{t}{t_{rise}}\right),\tag{80}$$

$$\frac{d\tilde{u}_g}{d\tilde{t}_g}=\frac{du_g}{dt_g}-\frac{u_p^{max}}{t_{rise}}\exp\left(-\frac{t}{t_{rise}}\right).\tag{81}$$

As the simulation time was sufficiently short to prevent wave interactions at $x=L$, no special modifications were required at that boundary. The well-known net effect of this non-Galilean transformation is simply to introduce a source term due to frame acceleration into the linear momentum equations. Upon completion of calculation, the results were transformed back into the laboratory frame, which is what is reported in Fig. 2. The equations of state are such that the shock moves faster in the solid as seen in Fig. 2, part B1. Once again, a high value of γ_g has been employed to allow simultaneous visualization of the wave dynamics. In Fig. 2, parts B2 and B3, expanded views are focused on the viscous shock layers. Here independent solutions of viscous shock
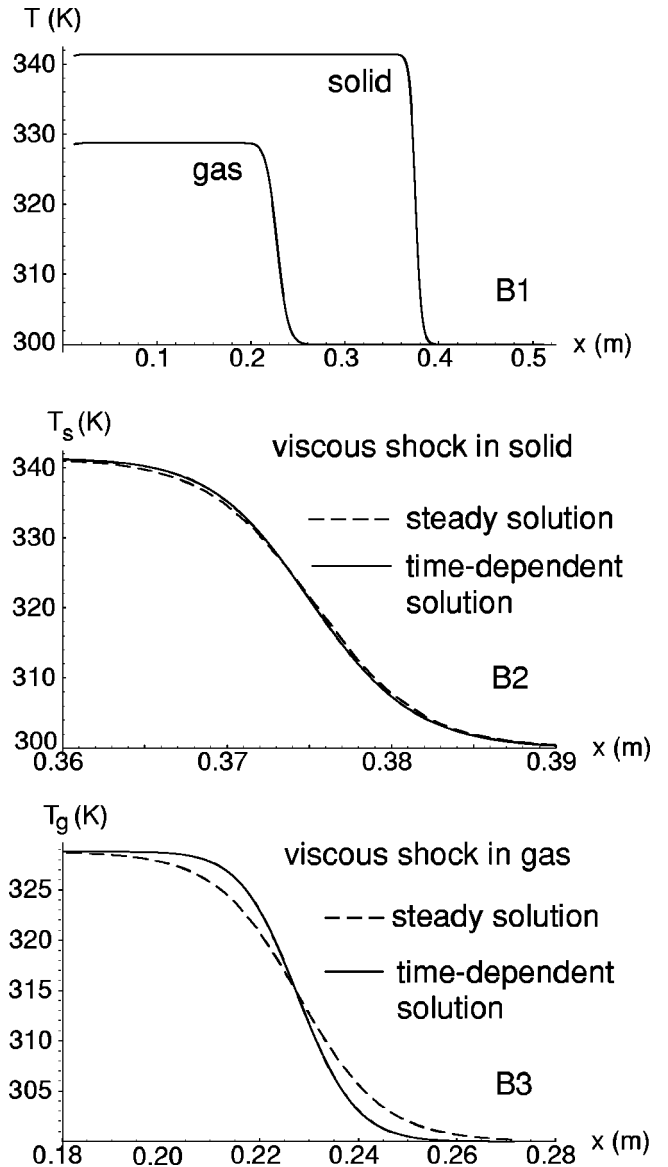

FIG. 2. Results for case B, piston driving into two noninteracting calorically perfect viscous ideal gases. (B1) Full spatial domain, (B2) expanded view of viscous shock in solid showing steady (dotted line) and unsteady (solid line) solutions, (B3) expanded view of viscous shock in gas showing steady (dotted line) and unsteady (solid line) solutions.

waves predicted by a steady state theory,[32] obtained from a numerical shooting method, are superposed. Again the results are remarkably good. In that the piston has translated away from its initial condition at $x=0$, the laboratory frame predictions are slightly displaced away from the origin. The preshock and postshock temperatures are nearly in exact agreement. The steady theory predicts wave speeds of 3153.74 m/s and 1847.85 m/s in the solid and gas, respectively. Rough estimates from the unsteady calculation obtained calculating the ratio of the x coordinate of the midpoint of the viscous structure to the local time yield predictions of 3125 m/s and 1917 m/s. The differences may be due to the effects of the finite rise time as well as difficulty in estimating the location of the smeared wave. The results also indicate that the unsteady model is capturing the correct length scales of diffusion. Both shocks in the gas and

solid are relaxing to the steady solution; the solid shock is relaxing at a faster rate, which explains why the gas shock shows a greater difference. Importantly, it is seen that the diffusion coefficients employed give rise to a gas shock thickness of roughly 6 cm and a solid shock thickness of roughly 3 cm. Consequently, roughly 300 particles of diameter 100 μm fit into the smallest length scale admitted by the continuum theory. It is noted that the simple diffusion model employed predicts a thinning of the shock width as the shock strength increases. This is consistent with the predictions of an experimentally validated Navier–Stokes model for gases.[33] Determination of whether such a result can be validated for granular materials would require consideration of a microstructural model not done here.

V. COMPACTION WAVE RESULTS

Next a series of simulations was performed for inert compaction waves. These results are similar to previously reported inviscid results for the solid phase only[7] and the solid and gas phases.[17] In these calculations, both solid and gas equations of state are nonideal with parameters appropriate to describe common heterogeneous materials. Three cases are studied to quantify the effects of the mechanisms of (C) compaction, (D) compaction and interphase drag, and (E) compaction, interphase drag, and interphase heat transfer. In each case the mixture with initial solid volume fraction of $\phi_{s0} = 0.73$ is driven by the same accelerating piston which quickly relaxes to a final velocity of 100 m/s, similar to that used in experiments.[1,34] Here the piston velocity is sufficiently small so as to induce waves which are subsonic with respect to the solid. A fourth calculation, F, considers a scenario nearly identical to E, except that the driving piston accelerates to a velocity of 1000 m/s. This induces a wave which is supersonic with respect to the solid. In order to resolve the finer structures induced by this more potent driver, five times as many computational cells are employed relative to all other cases.

A. Case C: Subsonic compaction

The mechanism of interphase compaction is activated by reducing the compaction viscosity μ_c to a finite value of 10^3 N s/m². Interphase drag and heat transfer are not activated. Predictions of pressures and configuration stress, solid volume fraction, velocities, and temperatures are shown in Fig. 3. Here clearly distinct disturbances in the solid and gas are predicted. In the solid, the disturbance is traveling at approximately 415 m/s and is associated with a increase in the volume fraction to a nearly completely packed solid with $\phi_s \sim 1$. The pressure in the solid rises from an ambient value of near 10 MPa to a compacted value of over 50 MPa. After a short delay in the compaction zone, the configurational stress β_s relaxes to a value close to that of the solid pressure, while the gas pressure is significantly lower. The thickness of the compaction zone is about 6 cm, thus it encompasses about 600 particles of 100 μm diameter. These values are quite close to values observed in experiment, as discussed in detail by Powers et al.[7] This wave, known as a compaction wave, is traveling at a much slower speed than the ambient

sound speed in the solid, which is around 3000 m/s, and as such it is not the limiting case of a shock wave. In fact, as demonstrated by corresponding inviscid theories, the structure of the compaction zone is dictated by the magnitude of μ_c, which despite its common name of "compaction viscosity," is in fact not associated with classical diffusion. In contrast, the precursor wave in the gas is traveling at a speed of around 830 m/s; its structure, which has thickness of about 4 cm, is dictated by the gas viscosity. As the ambient gas phase sound speed is 583.9 m/s, this wave is clearly a supersonic, viscous shock.

It is noted that the compaction wave speed is lower than the ambient sound speed in both phases. This is qualitatively consistent with well-known results obtained in special limit of pressure, temperature, and velocity equilibria,[26] but the quantitative agreement here is not strong. The quantitative disagreement is not surprising, as in this study, the two phases do not have equilibrated pressures.

The gas velocity is quite distinct from that of the solid, except that both relax to the piston velocity at the locus of the piston. Such velocity differences are not observed in experiment[24] and can be attributed to the neglect of interphase drag. The gas and solid temperatures are distinctly different as well, with large fluctuations noted in the gas phase temperature. The dynamics of the problem are such that the compaction induces the gas temperature to fall to a very low value in the compacted region of near 100 K. It is reasonable to attribute this to the neglect of interphase heat transfer.

B. Case D: Subsonic compaction and drag

In case D, the mechanisms of interphase compaction and drag are activated. A drag parameter of $\delta = 10^8$ kg/m³/s, of the same order of magnitude as suggested by experiment,[24] is employed, and results are shown in Fig. 4. Results for the solid phase are similar to those for case C. However, for the gas phase the introduction of drag has effectively equilibrated the gas velocity to that of the solid, brought the pressures much closer, and increased the temperature to around 330 K in the postcompaction zone. The shock wave is no longer discernible in the gas phase. While it appears that there is a temperature gradient and consequent heat flux at the piston face, examination of the results on a magnified scale reveals there is in fact a thin relaxation layer where the heat flux approaches zero for both phases.

C. Case E: Subsonic compaction, drag, and heat transfer

In case E, the mechanisms of interphase compaction, drag, and heat transfer are activated. By making a so-called Reynolds analogy that interphase drag and heat transfer are of the same order of magnitude, the heat transfer coefficient is estimated at $\mathcal{H} \sim \delta u_c^2 / T_c$, where the characteristic velocity and temperature are estimated to be $u_c \sim 100$ m/s and $T_c \sim 100$ K. This gives rise to an estimate of $\mathcal{H} = 10^{10}$ W/m³/K. Results are shown in Fig. 5. The results are essentially identical to those of case D, except that the solid and gas temperatures have relaxed to nearly identical values.
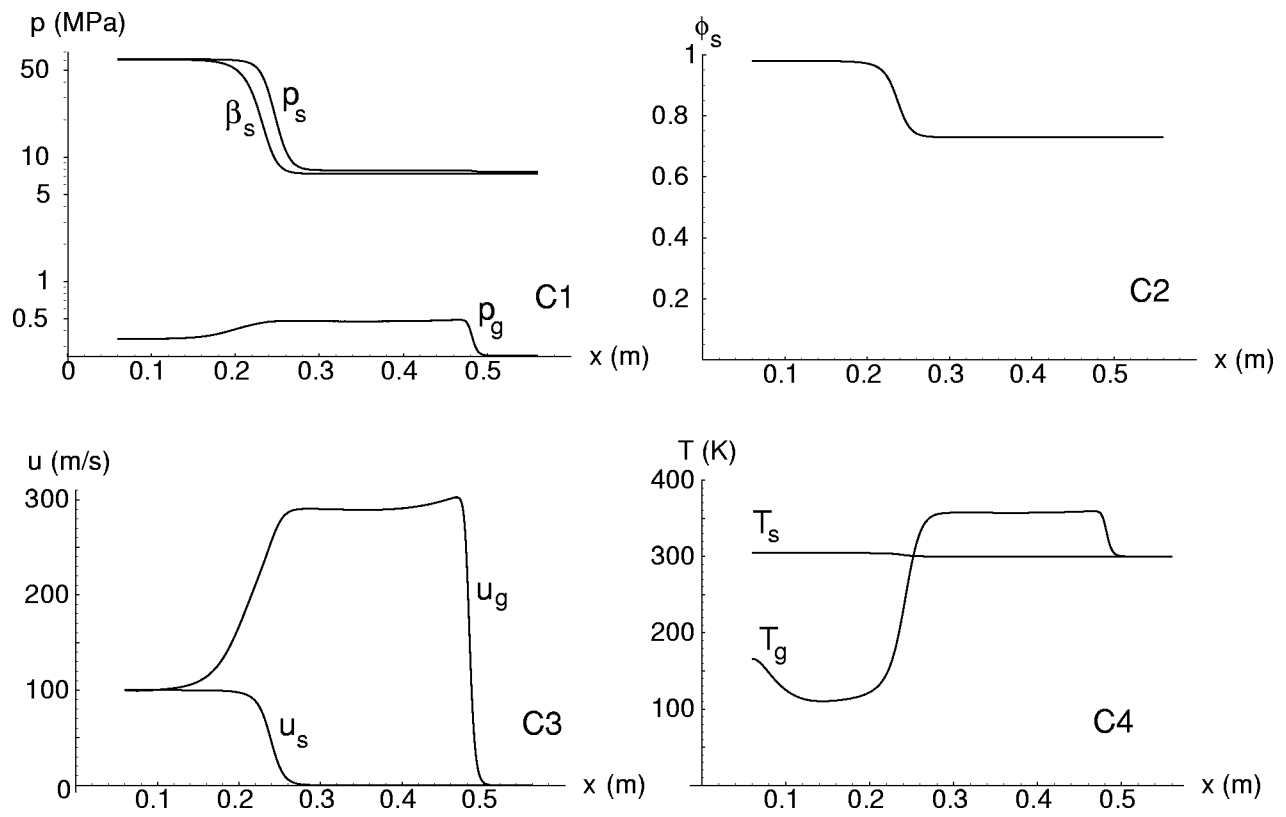
FIG. 3. Results for case C (piston-driven subsonic compaction): (C1) Solid and gas pressure and configuration stress profiles, (C2) solid volume fraction profile, (C3) velocity profiles, (C4) temperature profiles.
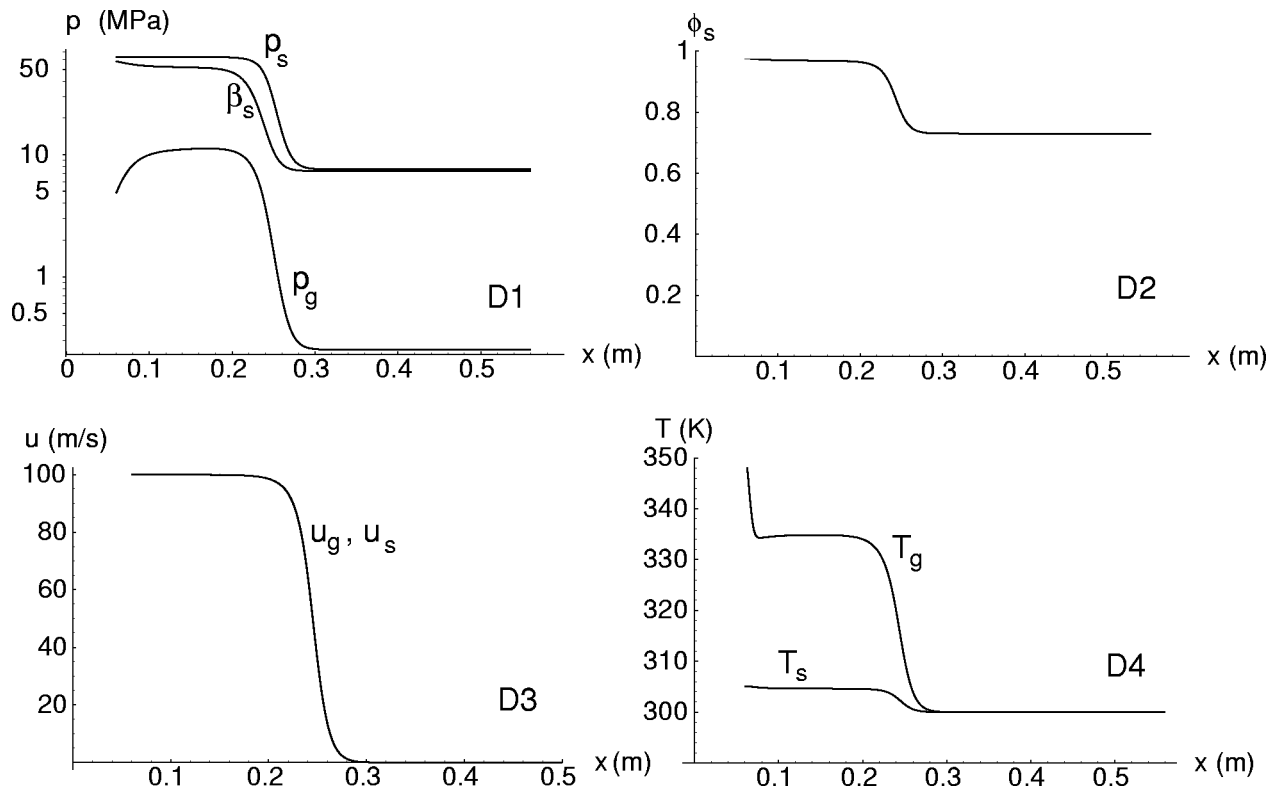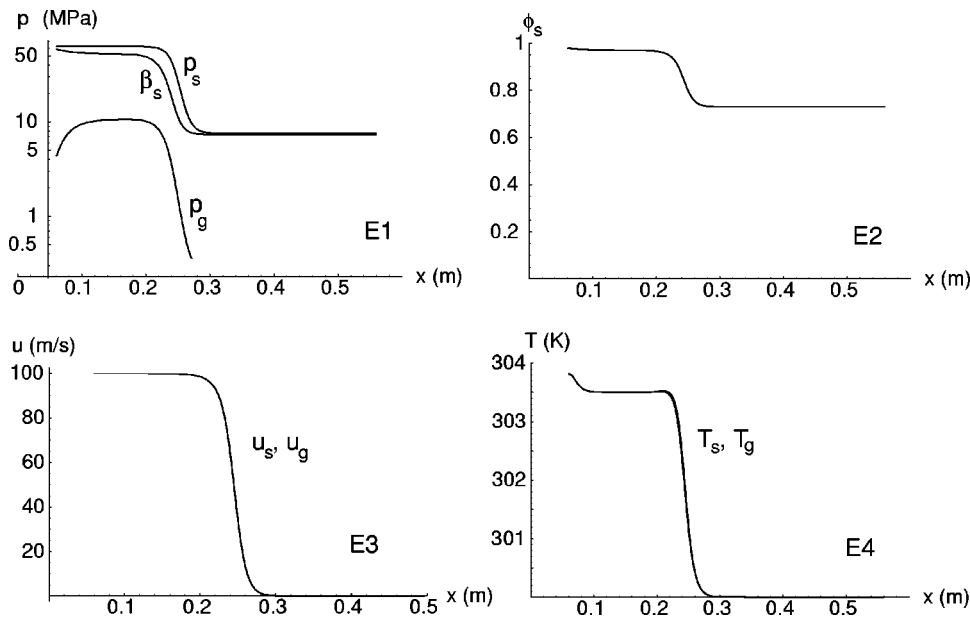

FIG. 4. Results for case D (piston-driven subsonic compaction with interphase drag): (D1) Solid and gas pressure and configuration stress profiles, (D2) solid volume fraction profile, (D3) velocity profiles, (D4) temperature profiles.

FIG. 5. Results for case E (piston-driven subsonic compaction with interphase drag, and heat transfer): (E1) Solid and gas pressure and configuration stress profiles, (E2) solid volume fraction profile, (E3) velocity profiles, (E4) temperature profiles.

As discussed in detail by Asay *et al.*,[24] these equilibration phenomena have important consequences when considering mechanisms which are likely to induce a transition to detonation in a reacting material. In particular, this model predicts that the compaction wave crushes the material to the extent that it would be difficult for reaction product gases to permeate ahead of the compaction wave to any significant degree. However, there remains a small amplitude of gas velocity which may be potentially important in a slow cookoff scenario. This rapid equilibration has motivated recent studies which replace evolution equations with algebraic constraints which force solid–gas equilibrium in order to reduce the computational stiffness associated with resolving thin layers.[19]

Predictions of an instantaneous budget of irreversibility production rate I are given for case E in Fig. 6. Here Eq. (63) is employed to calculate I as well as the magnitude of each of its constituents. In this case the peak entropy production rates for the various processes are all located in the region near $x = 0.3$ m, and have the following approximate peak magnitudes, given in rank order: interphase compaction,

1.75×10^8 W/m^3/K; solid momentum diffusion, 2.2×10^7 W/m^3/K; solid energy diffusion, 1.3×10^5 W/m^3/K; interphase momentum transfer, 3.4×10^4 W/m^3/K; gas momentum diffusion, 4.8×10^3 W/m^3/K; interphase energy transfer, 1.4×10^3 W/m^3/K; gas energy diffusion, 3.3×10^1 W/m^3/K. Obviously the bulk of the dissipation is focused in the solid phase, and the bulk of that is attributable to compaction. Momentum diffusion in the solid phase is the only other mechanism which makes a contribution of sufficient magnitude to be discerned in Fig. 6.

D. Case F: Supersonic compaction, drag, and heat transfer

In this case, each of the mechanisms active in case E remains active, and the same parameter values are employed, except the piston is driven ten times faster at 1000 m/s. A detailed steady inviscid analysis[7] reveals that at such speeds, compaction waves are described by a steady shock wave propagating faster than the ambient sound speed in the solid followed by an attached compaction zone in which all variables relax to their equilibrium values.

Predictions of solid pressure versus distance are shown in Fig. 7. In order to clearly display the structure of the wave, only a small portion, $x \in [0.020$ m,0.032 m$]$, of the entire domain $x \in [0$ m,0.5 m$]$ is depicted. The model predicts a wave of approximate thickness 0.0024 m propagating at an approximate velocity of 3250 m/s in which the pressure relaxes to a final value of 4566 MPa. Such a wave structure admits roughly 24 particles of size 100 μm within its relaxation zone. Other variables behave in a qualitatively similar manner as they did in case E in that solid and gas velocities as well as solid and gas temperatures are effectively equilibrated. The distinction between the shock and compaction zone is not apparent in Fig. 7. Had smaller diffusion coefficients been employed, this distinction would become discernible at the expense of rendering diffusive relaxation length scales to be smaller than the grain size.
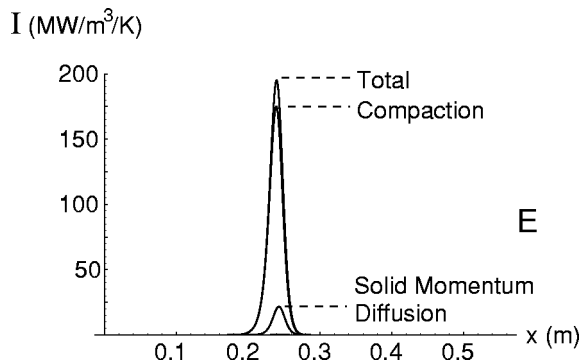

FIG. 6. Results for case E (piston-driven subsonic compaction with interphase drag and heat transfer): Total irreversibility production rate I and contributions from major components: interphase compaction and solid momentum diffusion.
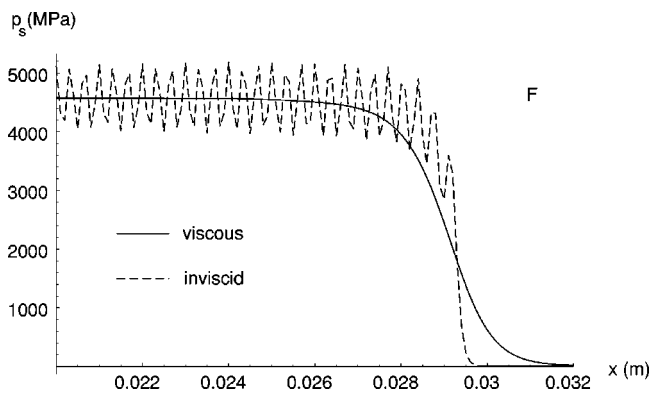
FIG. 7. Results for case F (piston-driven supersonic compaction with interphase drag, and heat transfer): Solid pressure predictions of the viscous theory (solid line) and corresponding inviscid equivalent (dashed line).

Superposed onto Fig. 7 are the predictions of an equivalent theory with all diffusion coefficients μ_s, μ_g, k_s, k_g set to zero. Here, the same simple second order spatial discretization scheme was used. As this discretization does not reduce to a first order scheme in the neighborhood of discontinuities, it is susceptible to pronounced dispersion effects which depend critically on the numerical resolution. These undesirable effects are readily seen in Fig. 7. For models which do not include nozzling and thus have a fully conservative form, the use of Godunov-based techniques for inviscid flows reduces the discretization to first order in the neighborhood of discontinuities and is able to crisply capture them without spurious oscillation.[10,17] For models which include nozzling, similar techniques can crisply capture jumps,[20] but questions remain as to whether the method has captured the correct jumps.[19]

Predictions of an instantaneous budget of irreversibility production rate I are given for case F in Fig. 8. In this case the peak entropy production rates for the various processes are all located in the region near $x = 0.028$ m, and have the following approximate peak magnitudes, given in rank order: interphase compaction, 1.9×10^{12} W/m^3/K; solid momentum diffusion, 3.2×10^{11} W/m^3/K; solid energy diffusion, 1.2×10^{11} W/m^3/K; interphase energy transfer, 1.5×10^8 W/m^3/K; gas momentum diffusion,
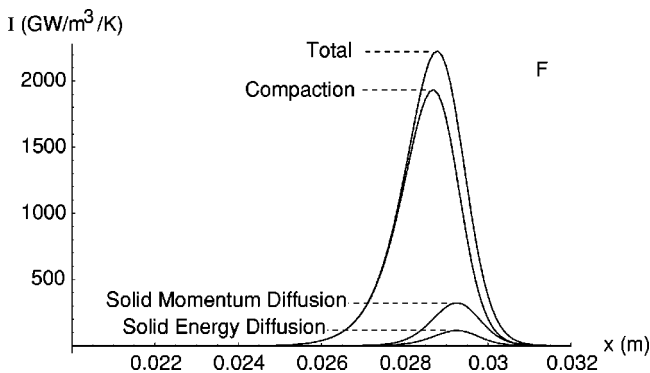

FIG. 8. Results for case F (piston-driven supersonic compaction with interphase drag and heat transfer): Total irreversibility production rate I and contributions from major components: interphase compaction, solid momentum diffusion, and solid energy diffusion.

8.8×10^7 W/m^3/K; gas energy diffusion, 2.5×10^7 W/m^3/K; interphase momentum transfer, 1.6×10^7 W/m^3/K. Again, the bulk of the dissipation is focused in the solid phase, and the bulk of that is attributable to compaction. Momentum and energy diffusion in the solid phase are the only other mechanisms which makes a contribution of sufficient magnitude to be discerned in Fig. 8. One also notes that the dissipation due to diffusion is at the leading edge of the disturbance, while that due to compaction trails slightly. This is consistent with the predictions of an inviscid theory which has a leading shock followed by a compaction zone.

VI. DISCUSSION

This study has shown that it is possible to introduce diffusion in a rational manner to models of heterogeneous energetic solids. With this extension, it has been demonstrated that real advantages exist relative to inviscid models. First, at the expense of computing on a sufficiently fine grid to resolve all diffusive structures, one can apply relatively simple numerical methods to nonconservative formulations of the governing equations. Second, the presence of a small finite length scale on which dissipation occurs can prevent unphysical instabilities predicted by inviscid models when they are subjected to grid resolution. Third, as these calculations were resolved with modest modern computational resources with no adaptive mesh refinement, it may be appropriate for the modeling community to reconsider if the traditional reasons for routinely neglecting diffusion are always applicable. Fourth, the modeler has gained control, independent of the particular numerical method chosen, over the width of the small scale structures, which should never be below that of the grain scale, as they can be for inviscid models.

Exercise of this model has demonstrated that it is converging at the proper order, and that appropriate boundary conditions have been imposed to guarantee the initial boundary value problem is well posed. Predictions of compaction wave structures demonstrate good agreement with known results and verify the critical role of compaction in introducing irreversible energy transfer, which could induce combustion, into the solid phase.

A challenge which is unmet, however, is to provide a rigorous granular subscale physical justification for the the critical constitutive theories required by this and all continuum mixture models in a fashion similar to that which has been provided from the kinetic theory of gases. All present macroscale models of deflagration-to-detonation transition are validated by tuning model parameters so as to be able to replicate limited experimental data sets. While this approach has value in interpolating within the confines of the experimental data base, it may not work well outside the bounds of the experiments. Consequently, without a more fundamental theory, the best of ongoing and important national efforts to improve both computational hardware and algorithms provide a necessary, but insufficient, step towards a theory which truly predicts the behavior of energetic granular materials.

ACKNOWLEDGMENTS

[1] H. W. Sandusky and R. R. Bernecker, "Compressive reaction in porous beds of energetic materials," in Eighth (International) Symposium on Detonation, Albuquerque, NM, 15 July 1985, pp. 881–891.

[2] J. M. McAfee, B. Asay, W. Campbell, and J. B. Ramsay, "Deflagration to detonation in granular HMX," in Ninth (International) Symposium on Detonation, Portland, OR, 28 August 1989, pp. 265–279.

[3] S. S. Gokhale and H. Krier, "Modeling of unsteady two-phase reactive flow in porous beds of propellant," Prog. Energy Combust. Sci. **8**, 1 (1982).

[4] P. B. Butler and H. Krier, "Analysis of deflagration to detonation transition in high-energy solid propellants," Combust. Flame **63**, 31 (1986).

[5] M. R. Baer and J. W. Nunziato, "A two-phase mixture theory for the deflagration-to-detonation transition in reactive granular materials," Int. J. Multiphase Flow **12**, 861 (1986).

[6] M. R. Baer, "Numerical studies of dynamic compaction of inert and energetic granular materials," J. Appl. Mech. **55**, 36 (1988).

[7] J. M. Powers, D. S. Stewart, and H. Krier, "Analysis of steady compaction waves in porous materials," J. Appl. Mech. **56**, 15 (1989).

[8] J. M. Powers, D. S. Stewart, and H. Krier, "Theory of two-phase detonation—part I: modeling," Combust. Flame **80**, 264 (1990).

[9] J. M. Powers, D. S. Stewart, and H. Krier, "Theory of two-phase detonation—part II: structure," Combust. Flame **80**, 280 (1990).

[10] K. A. Gonthier and J. M. Powers, "A numerical investigation of transient detonation in granulated material," Shock Waves **6**, 183 (1996).

[11] A. K. Kapila, S. F. Son, J. B. Bdzil, R. Menikoff, and D. S. Stewart, "Two-phase modeling of DDT: Structure of the velocity-relaxation zone," Phys. Fluids **9**, 3885 (1997).

[12] R. Pape and D. Gidaspow, "Numerical simulation of intense reaction propagation in multiphase systems," AIChE J. **44**, 294 (1998).

[13] R. Saurel and J. Massoni, "On Riemann-problem-based methods for detonations in solid energetic materials," Int. J. Numer. Methods Fluids **26**, 101 (1998).

[14] J. B. Bdzil, R. Menikoff, S. F. Son, A. K. Kapila, and D. S. Stewart, "Two-phase modeling of deflagration-to-detonation transition in granular materials: A critical examination of modeling issues," Phys. Fluids **11**, 378 (1999).

[15] J. Massoni, R. Saurel, G. Baudin, and G. Demol, "A mechanistic model for shock initiation of solid explosives," Phys. Fluids **11**, 710 (1999).

[16] R. Saurel and R. Abgrall, "A multiphase Godunov method for compressible multifluid and multiphase flows," J. Comput. Phys. **150**, 425 (1999).

[17] K. A. Gonthier and J. M. Powers, "A high-resolution numerical method for a two-phase model of deflagration-to-detonation transition," J. Comput. Phys. **163**, 376 (2000).

[18] R. Saurel and O. Lemetayer, "A multiphase model for compressible flows with interfaces, shocks, detonation waves and cavitation," J. Fluid Mech. **431**, 239 (2001).

[19] A. K. Kapila, R. Menikoff, J. B. Bdzil, S. F. Son, and D. S. Stewart, "Two-phase modeling of deflagration-to-detonation transition in granular materials: Reduced equations," Phys. Fluids **13**, 3002 (2001).

[20] R. Abgrall and R. Saurel, "Discrete equations for physical and numerical compressible multiphase mixtures," J. Comput. Phys. **186**, 361 (2003).

[21] K. A. Gonthier, "Modeling and analysis of reactive compaction for granular energetic solids," Combust. Sci. Technol. **175**, 1679 (2003).

[22] L. Sainsaulieu, "Traveling waves solution of convection-diffusion systems whose convection terms are weakly nonconservative: Application to the modeling of two-phase fluid flows," SIAM (Soc. Ind. Appl. Math.) J. Appl. Math. **55**, 1552 (1995).

[23] J. von Neumann and R. D. Richtmyer, "A method for the numerical calculation of hydrodynamic shocks," J. Appl. Phys. **21**, 232 (1950).

[24] B. W. Asay, S. F. Son, and J. B. Bdzil, "The role of gas permeation in convective burning," Int. J. Multiphase Flow **22**, 923 (1996).

[25] J. B. Bdzil, R. Engelke, and D. A. Christenson, "Kinetics study of a condensed detonating explosive," J. Chem. Phys. **74**, 5694 (1981).

[26] D. A. Drew and S. L. Passman, *Theory of Multicomponent Fluids* (Springer, New York, 1998).

[27] H.-O. Kreiss and J. Yström, "Parabolic problems which are ill-posed in the zero dissipation limit," Math. Comput. Modell. **35**, 1271 (2002).

[28] E. Zauderer, *Partial Differential Equations of Applied Mathematics* (Wiley, New York, 1989).

[29] T. J. Poinsot and S. K. Lele, "Boundary conditions for direct simulations of compressible viscous flows," J. Comput. Phys. **101**, 104 (1992).

[30] A. C. Hindmarsh, "ODEPACK, a systematized collection of ODE solvers," in *Scientific Computing* (North-Holland, Amsterdam, 1983), pp. 55–64.

[31] A. H. Shapiro, *The Dynamics and Thermodynamics of Compressible Flow* (Kreiger, Malabar, FL, 1953), Vol. 2.

[32] R. von Mises, "On the thickness of a steady shock wave," J. Aeronaut. Sci. **17**, 551 (1950).

[33] H. W. Liepmann and A. Roshko, *Elements of Gasdynamics* (Wiley, New York, 1957).

[34] H. W. Sandusky and T. P. Liddiard, "Dynamic compaction of porous beds," NSWC TR Report No. 83-256, 1985.